Journal of Alloys and Compounds 1080 (2026) 190290

Contents lists available at ScienceDirect

Journal of Alloys and Compounds

journal homepage: www.elsevier.com/locate/jalcom

Research article

Influence of Ni, Cr and Ni-Cr20 coatings on the electrochemical parameters and corrosion behaviour of Ni–Fe–Cu anodes at 800 °C under aluminium electrolysis conditions

Thomas Jamieson [a,*,1], Ronja Anton [b,*,1], Andrey Yasinskiy [c], Roman Düssel [c], Ralf Busch [d], Uwe Schulz [b], Bernd Friedrich [e], Isabella Gallino [a]

[a] Technical University of Berlin, Ernst-Reuter-Platz 1, Berlin 10587, Germany
[b] German Aerospace Center (DLR), Institute for Frontier Materials on Earth and in Space, Linder Höhe, Cologne 51147, North-Rhine Westphalia, Germany
[c] TRIMET Aluminium SE, Aluminiumallee 1, Essen 45356, North-Rhine Westphalia, Germany
[d] Saarland University, Campus, Saarbrücken 66123, Germany
[e] IME Process Metallurgy and Metal Recycling, Intzestraße 3, Aachen 52056, North-Rhine Westphalia, Germany

ARTICLE INFO

Keywords:
Coatings
Molten salt corrosion
Kinetics
Inert anodes
Alloys

ABSTRACT

The electrochemical corrosion behaviour of uncoated, Ni, Ni-Cr20 and Cr-coated $Ni_{42}Fe_{38}Cu_{20}$ wt.% anodes was investigated with respect to corrosion current density, wear rate and scale morphology in a NaF-KF-AlF_3-Al_2O_3 melt at 800 °C, for up to 1 h of electrolysis. Ni-Cr20 and Cr-coated anodes were found to be the most resistant to oxidation in air due to Cr_2O_3 formation and reduced interdiffusion with substrate elements, whereas Ni-coated anodes demonstrated significant interdiffusion and oxide penetration. Electrochemical measurements of exchange current densities on the clean and oxidised anode surface were used to calculate the wear rate (WR), where the Ni-Cr20 coating was deemed to be detrimental to anode performance due to the catastrophic tendency towards electrode passivation via NiF_2 formation. For the Ni and Cr-coated anodes, whilst a slight increase in the electrochemical parameters and wear rates was observed compared to their uncoated counterparts, SEM-EDX analysis of used-anode cross-sections revealed a significant reduction in electrolyte penetration for these two coatings as well as the formation of a more uniform oxide scale with less extensive blistering. Overall, the increase in corrosion parameters for the Ni and Cr-coated anodes appears to derive from the sacrificial dissolution of the coating material, whilst a noticeable degree of protection to the bulk is provided. The longer-term corrosion resistance implications with respect to changes in corrosion scale and desirable $NiFe_2O_4$ formation are discussed, and a robust research methodology for future studies on suitable coatings for inert anodes is displayed.

1. Introduction

To date, the primary production of aluminium via the Hall–Héroult process relies on consumable carbon anodes. Continuous oxygen evolution at the anode surface results in the emission of approximately 1.5 t of CO_2 per tonne of aluminium produced: $2Al_2O_3(sol) + 3C(s) \rightarrow 4Al(l) + 3CO_2(g)$. Perfluorocarbons (PFCs) production also presents a concern, with approximately ~6 Mt CO_2e emitted in 2023 [1]. Replacing the carbon anode with an inert anode (oxygen-evolving anode) alternative would eliminate direct green house gas (GHG) emissions from the electrolysis process. Various attempts have been made using metallic, ceramic, and cermet anodes [2–14]. At present however, no replacement has been found that can adequately substitute carbon anodes.

Metallic Ni–Fe–Cu anodes have attracted significant interest due to their tendency to form a surface layer rich in $NiFe_2O_4$ during oxidation, which exhibits low solubility in cryolite-based melts [4,15,16]. A range of compositions have been investigated [4–8,17–19] with the overall aim of improving anode lifespan via altering the alloy design. For metallic anodes in particular, corrosion resistance remains the limiting factor as other prerequisites such as good conductivity, ease of production and good thermal shock resistance are satisfied. Whilst varying the alloy design has typically been employed to improve the intrinsic corrosion behaviour of Ni–Fe–Cu anodes, the application of surface

* Corresponding authors.
E-mail addresses: t.jamieson@campus.tu-berlin.de (T. Jamieson), Ronja.Anton@dlr.de (R. Anton).
[1] Thomas Jamieson and Ronja Anton contributed equally to this work and share first authorship.

https://doi.org/10.1016/j.jallcom.2026.190290
Received 7 April 2026; Received in revised form 22 June 2026; Accepted 5 August 2026
Available online 12 August 2026
0925-8388/© 2026 The Authors. Published by Elsevier B.V. This is an open access article under the CC BY license (http://creativecommons.org/licenses/by/4.0/).

coatings has recently emerged as a complementary approach to further improve corrosion resistance [20,21]. Applying a protective coating has been postulated to offer early-stage protection, allowing a more stable $NiFe_2O_4$ layer to form underneath, thereby extending anode lifespan [21]. Recent work has explored the use of (Co,Ni)O spinel coatings to improve corrosion resistance and promote the formation of a coherent $NiFe_2O_4$ layer in Cu-rich compositions, both with and without a Ni–Cr20 bond coat [20,21]. [Ni–Cr + (Co,Ni)O] coated Cu-rich alloys demonstrated poor corrosion resistance due to coating delamination whereas pure (Co,Ni)O coatings were reported to enhance short-term corrosion resistance [21].

Corrosion resistance is a complex and crucial parameter for alloys designed for CO_2-free aluminium electrowinning. In practice, it is more common to use a wear rate to evaluate the performance of the anode. The wear rate can be found in a mass-balance experiment by evaluating the masses of anode constituents in the resultant aluminium after a certain time of electrolysis under preselected "standard" conditions that include a certain temperature, current density, geometry and design of the cell. The accuracy and reproducibility increase with the electrolysis time and size of the cell (and corresponding total current). It was demonstrated [17] that certain electrochemical parameters have a strong linear correlation with the wear rate and can be used to evaluate the corrosion resistance of the alloy in a more practical and convenient manner. The electrochemical measurements can be conducted much faster than the electrolysis test and require fewer materials. Additionally, it is easier to maintain a controlled and consistent environment. While the electrolysis tests can help to understand the overall resulting wear rate, the electrochemical measurements can address different stages and mechanisms of the corrosion. At least four mechanisms responsible for the overall wear of the anode can be distinguished. The first one, electrochemical metal dissolution, dominates when the oxidation product is liquid or partially liquid. This is often true for fluorides that have low melting temperatures and high solubility in molten cryolite. Additionally, the potential difference between oxide formation and fluoridation is rather small for many metals. For instance, the difference in standard potentials between FeO and FeF_2 is less than 20 mV for a wide range of temperatures. For these reasons, metal dissolution in most cases occurs as fluoridation. The fluoridation rate depends on:

- the surface area of the metal exposed to the melt, which is controlled by the properties of the oxide scale normally deposited on the surface of the anode during the electrolysis;
- temperature;
- content of dissolved oxides (oxidised anode material & alumina) at the surface of the metal controlled by the bulk concentration, anodic current density and transport properties of the melt;
- nature of the metal and structure of the anode.

The second mechanism is the chemical dissolution of the oxide scale, which follows the reaction:

$$3n\mathrm{MeO_n} + 2n\mathrm{AlF_3} = 3n\mathrm{MeF_{2n}} + n\mathrm{Al_2O_3} \quad (1)$$

The rate of oxide dissolution is affected by:

- surface area of the oxide scale exposed to the melt, which is affected by the macroscopic properties of the scale, such as open porosity;
- oxide solubility in the molten salt, which is controlled by the nature and structure of the oxide, melt composition and temperature;
- dissolved oxide concentration at the surface of the oxide scale, which is controlled by the anodic current density, aluminium oxide concentration, transport properties and fluid dynamics in the melt.

The third mechanism, the electrical passivation, happens when the reaction product possesses insulating properties and has, at the same time, a high melting temperature. This is often observed in anodes with high Ni content, when NiF_2 deposits between the oxide scale and the metallic surface of the anode and leads to a current redistribution between the remaining active surface area. The increased local current density increases the rate of further passivation and metal fluoridation. The rate of passivation depends on the same factors as the fluoridation. The fourth mechanism is the oxide scale macroscopic breakdown. It happens due to the insufficient properties of the scale or a weak adhesion of the scale to the metal. In this work, the first three mechanisms were addressed and evaluated using the electrochemical methods.

A thorough investigation into the role of Ni, Cr, and Ni–Cr20 coatings on the corrosion mechanism of highly alloyed $Ni_{42}Fe_{38}Cu_{20}$ wt. % anodes is presented here, with the aim of assessing whether metallic surface engineering alone can improve the short-term stability of metallic inert anodes. $Ni_{42}Fe_{38}Cu_{20}$ wt. % was selected as the substrate because single-phase alloys of this composition have previously shown promising behaviour during aluminium electrolysis trials [5–8]. Unlike most prior studies on Ni–Fe–Cu inert anodes, which have focused primarily on modifying bulk alloy composition, this work places the emphasis on the deposited coating itself as an additional and potentially enabling design variable. In this context, coatings are of particular interest because they may provide early-stage protection against fluoridation and oxide-scale destabilisation, thereby delaying degradation and promoting the establishment of a more protective surface layer.

Previous coating studies on metallic inert anodes have largely focused on thermally sprayed or plasma-sprayed coatings investigated by Jalilvand et al. [20,21]. In contrast, the present work explores magnetron sputter deposition of metallic Ni, Cr, and Ni–Cr20 coatings on $Ni_{42}Fe_{38}Cu_{20}$ substrates. The use of sputter-deposited coatings is relevant because it enables the production of thin, dense, and compositionally controlled layers, offering a different pathway from plasma-sprayed coatings for influencing interfacial reactions during the initial stages of electrolysis.

Accordingly, this study examines whether sputter-deposited metallic coatings can improve the corrosion resistance of $Ni_{42}Fe_{38}Cu_{20}$ anodes in cryolite-based melts, and how these coatings modify the first three wear mechanisms identified above. Ni, Cr, and Ni–Cr20 coatings were deposited by magnetron sputtering onto homogenised $Ni_{42}Fe_{38}Cu_{20}$ wt. % anodes and evaluated in small-scale electrolysis cells with 1 h runtimes, alongside an uncoated control group. In parallel, the coating materials were also examined as monolithic anodes, allowing the intrinsic reaction and corrosion behaviour of the coating compositions to be separated from substrate-coating interaction effects. SEM and EDX were used to assess coating integrity, scale adhesion, and corrosion behaviour, complemented by electrochemical measurements. By focusing on metallic coatings without an additional spinel top layer, this work aims to clarify both the protective potential and the limitations of sputter-deposited surface layers as a complementary strategy to alloy design for the development of longer-lasting inert anodes.

2. Experimental

2.1. Sample preparation

Preparation of the $Ni_{42}Fe_{38}Cu_{20}$ wt%, bulk Ni–Cr20 and pure Ni alloys began with the synthesis of the alloys from constituent nickel, iron, copper and chromium (≥99.95 wt% purity) in a custom-made arc-melter. The correct amounts of the constituent elements were determined with a fine balance, before being melted together in a pre-cleaned vacuum-cycled (10^{-3} mbar) argon atmosphere (~0.2 bar). The alloys were flipped and melted four times in total, evenly on each side, to ensure an even distribution of the constituent metals. The alloys were then cast into cylindrical forms 45 mm in length and 7 mm in

diameter using an Indutherm MC15 tilt-caster under a vacuum-cycled (10^{-2} mbar) argon atmosphere (~0.1 bar). Casting was performed into a water-cooled copper mould. Finally, all the cast $Ni_{42}Fe_{38}Cu_{20}$ wt% alloys were annealed in a Nabetherm vertical furnace to obtain a homogeneous microstructure. The furnace was heated to 1100 °C at a heating rate of 0.2 °C/s and held for 12 h before cooling in the furnace. Metallographic preparation was performed, along with an aqueous ferric chloride etchant, prior to optical microscopy analysis to confirm the presence of the single-phase microstructure on a separate $Ni_{42}Fe_{38}Cu_{20}$ wt% sample prepared under identical conditions.

Finally, the annealed samples were machined to a 40 mm long custom rod of ϕ4 mm with a screw hole. For the active component, to be coated and used for electrolysis, a length of 20 mm was machined down even further to produce a ϕ2 mm pin to be partially submerged in the electrolyte, complete with a 120 grit surface finish. For preliminary coating tests, rods with a 6 mm diameter were machined from the as-cast 7 mm casts.

2.2. Coating deposition analytics

The coatings were fabricated using a batch-type magnetron sputtering system (Z 400, Systec SVS Vacuum Coatings, Karlstadt, Germany). Prior to coating deposition, Ar^+-ion etching was performed to clean and activate the surface of the specimen. Dense polycrystalline Cr and Ni disks, each with a diameter of 100 mm, were used as targets and arranged in a face-to-face configuration. DC and DC/RF co-sputtering were carried out at varying target powers to produce coatings with different compositions: 100 at% Cr (Cr), 100 at% Ni (Ni), and 80 at% Ni with 20 at% Cr (Ni–Cr20). The total pressure during deposition was maintained at 0.47 Pa in an Ar atmosphere with a flow rate of 23 sccm. The deposition rates were approximately 11.5 µm/h for the Cr coating, 4.5 µm/h for the Ni coating, and 6.3 µm/h for the Ni–Cr20 coating. The rotation speed during deposition was 12 min^{-1}.

For preliminary investigations of the coatings, rods of ϕ6 mm were cut into smaller pieces for coating, testing, and analysis under varying parameters. Although these samples underwent a twofold rotation during deposition, they could not be coated uniformly due to shading effects. These effects were not present in the final rod samples, as they were mounted in a different way. One piece from each coated sample was subjected to a heat treatment in a vacuum furnace at 800 °C for 1 h. To further evaluate the oxidation behaviour, an additional oxidation test was performed in ambient air for one hour at 800 °C, both on a vacuum-treated sample and an as-deposited sample. One specimen from each coating type was retained in the as-deposited condition, without any thermal treatment, to serve as a reference for post-deposition analysis. Based on the oxidation results, the most promising coating condition was selected and subsequently applied to the rods intended for electrolysis testing.

Several analytical techniques were employed to characterise the coatings. X-ray diffraction (XRD) analysis was conducted using a Bruker D8 Advance diffractometer with Cu Kα radiation and Co Kα radiation, and data evaluation was performed using the EVA/Topas 4.2 software package (Bruker AXS, Karlsruhe, Germany). This allowed for identification of the crystalline phases and tracking of phase evolution after coating deposition and subsequent oxidation. The XRD-scans themselves are not included as figures, the results are incorporated in the text but can be made available upon request. Surface morphology was investigated using a scanning electron microscope (SEM) (DSM Ultra 55, Carl Zeiss NTS, Wetzlar, Germany) operated at 5 kV. To complement the XRD data and determine local composition, energy-dispersive X-ray spectroscopy (EDX) was performed using the Aztec system (Oxford Instruments, Abingdon, UK) at an accelerating voltage of 15 kV.

The specimens tested in the electrolysis bath were also analysed using SEM; however, XRD analysis was not possible due to the small diameter and geometry of the rod-shaped samples.

Table 1
Overview of the anode types investigated in this study.

Substrate/bulk alloy	Coating type	No. of anodes measured
$Ni_{42}Fe_{38}Cu_{20}$	–	2
$Ni_{42}Fe_{38}Cu_{20}$	Ni	3
$Ni_{42}Fe_{38}Cu_{20}$	Cr	3
$Ni_{42}Fe_{38}Cu_{20}$	Ni–Cr20	3
Ni	–	3
Ni–Cr20	–	3

2.3. Electrochemical measurements

Experiments were conducted in the low-temperature NaF-KF-AlF_3–$Al_2O_{3(sat)}$ melt with cryolite ratio CR = 1.3 and potassium ratio KR = 0.32 at 800 ± 2 °C. The bath was prepared using dried NaF and KF salts, each with a purity of 99.5% supplied by Sigma-Aldrich. Industrial-grade AlF_3 and smelter-grade alumina, serving as a source of O_2-ions, were provided by Trimet Aluminium SE (Germany). Electrochemical measurements were carried out in a three-electrode cell (Fig. 1), consisting of a graphite container containing approximately 300 g of electrolyte, placed within a gas-tight steel reactor. The reactor had a continuous Ar supply and a water-cooled lid. The 20 mm × ϕ2 mm pin was immersed 10 mm deep in the electrolyte and served as the working electrode. The quasi-reference electrode (qRE) was a ϕ1 mm tungsten rod, also immersed 10 mm deep in the electrolyte. The counter electrode was a ϕ4 mm glassy carbon rod, immersed 20 mm deep. Temperature measurements were conducted using an S-type thermocouple immersed 10 mm deep (see Table 1).

Corrosion resistance of the alloys was characterised using the method proposed and explained in [17]. Electrochemical kinetic parameters, correlated with different corrosion mechanisms, were recorded using an Iviumstat.h potentiostat (Ivium Technologies, The Netherlands) controlled by Iviumsoft, following the steps summarised in Table 2.

Each sample type was tested three times to confirm reproducibility. The exchange current density was determined by extrapolating the linear portions of the Tafel plot to the reversible potential (Fig. 2). The average between the cathodic (left) arm and the anodic (right) arm was calculated.

Stationary potentials were graphically determined from the potential-time curve recorded during the chronopotentiometry (galvanostatic polarisation) (Fig. 3).

For the purposes of this study, wear rate (WR) refers to the material loss of the anode [17]. The wear rate WR (in g/cm^2 s) was calculated using the following empirical equation:

$$\mathrm{WR} = a\left(\frac{M'}{z'F}\right)\left(b\,i_{0(\mathrm{cl})} + i_{0(\mathrm{ox})}\right) \tag{2}$$

where $a = 4.54 \cdot 10^{-3}$ is the first dimensionless empirical constant, M' = 58.7 g mol^{-1} is the apparent molar mass (Ni), z' = 2 is the apparent number of electrons (Ni), F = 96485 C mol^{-1} is the Faraday constant, b = 15.5 is the second dimensionless empirical constant, $i_{0(\mathrm{cl})}$ [A cm^{-2}] is the exchange current density on the clean anode and $i_{0(\mathrm{ox})}$ [A cm^{-2}] is the exchange current density on the oxidised anode. Cross-sections of the submerged portions of the used anodes were examined by SEM and EDX to quantify the corrosion scale thickness and the extent of electrolyte penetration beneath the scale, while also characterising the reaction products within the scale.

3. Results

3.1. Coatings of alloys

The Ni coating exhibits a typical columnar structure after deposition, as shown in Fig. 4a. It reveals straight and fine columnar grains

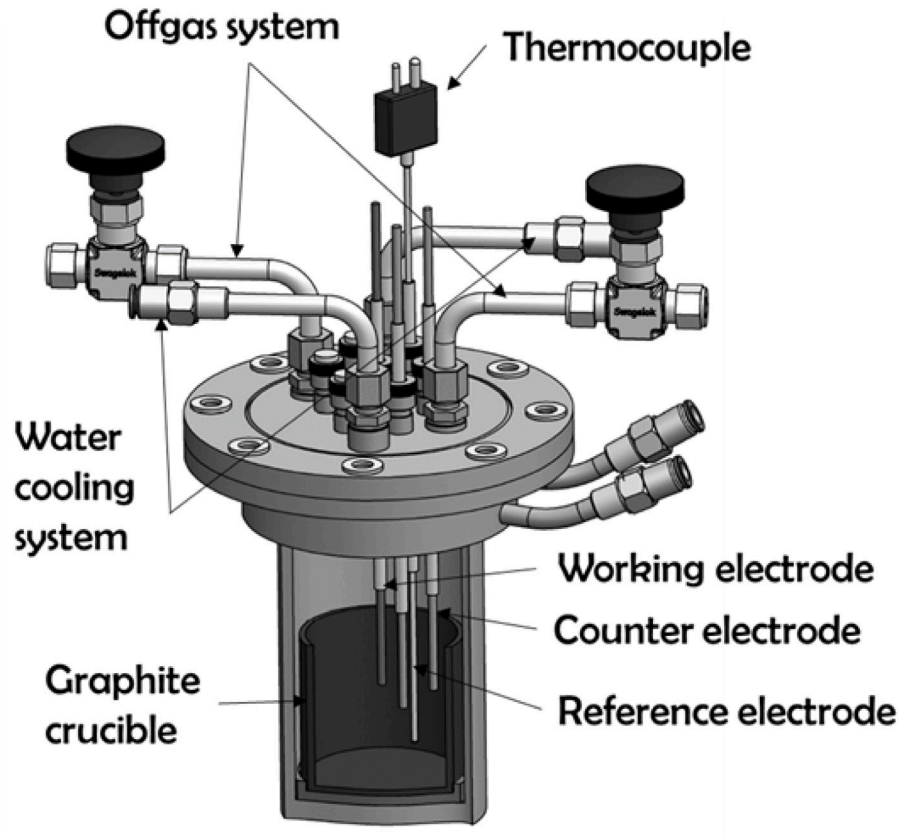


Fig. 1. Electrochemical set-up.

Table 2
Electrochemical measurement protocol. LSV: linear sweep voltammetry.

#	Procedure	What is measured	What is characterised
1	Equilibration time (3 min)	Open circuit potential	–
2	LSV[a] after immersion	Exchange current and reversible potential on a clean anode	Resistance to metal dissolution/fluoridation
3	Galvanostatic polarisation (1 h, $i = 0.1$ A cm^{-2})	Stationary potential	Oxide layer growth and passivation behaviour
4	LSV after polarisation	Exchange current and reversible potential on an oxidised anode	Resistance to oxide dissolution

[a] Linear sweep voltammetry (potential range: $E_{ocp} \pm 300$ mV, sweep rate 50 mV s^{-1}).

with a thickness of about 9.5 μm. XRD analysis confirmed that the coating is crystalline in the as-deposited state.

After vacuum treatment for 1 h at 800 °C, the Ni coating completely interdiffused with the base alloy. Fe and Cu diffused into the coating, while Ni diffused into the alloy. As a result, the original columnar structure was no longer visible, and the coating bonded entirely to the alloy. When additionally exposed for 1 h in laboratory air at 800 °C, a thermally grown oxide (TGO) was formed, consisting of two distinct regions (Fig. 4b). The upper layer is rich in iron oxide with nickel oxide precipitates, whereas the lower layer is rich in nickel oxide. XRD analysis also confirms the presence of $NiFe_2O_4$, NiO, and Fe_2O_3. Along the former intercolumnar boundaries, iron oxides formed. The total TGO thickness was approximately 5.5 μm. The coating adhered firmly to the alloy, and no oxidation of the underlying alloy was detected.

The coating shown in Fig. 4c, tested in laboratory air for 1 h immediately after deposition, also developed a two-layered TGO with a similar oxide distribution. The oxide scale thickness was comparable to that of the vacuum-treated coating. Horizontal iron oxide growth was observed along the former intercolumnar gaps, which were sealed during oxidation. Cu and Fe diffusion into the coating was also evident. Despite these changes, the coating was well-adhered to the alloy and preserved a dense morphology.

The Cr coating exhibits a fine columnar structure similar to that of the Ni coating, although the columns bend at approximately one-third of the coating thickness, as shown in Fig. 5a. The coating adheres firmly to the alloy and has a thickness between 9.5 μm and 13.5 μm. XRD analysis confirmed that the coating is crystalline in the as-deposited state.

After vacuum treatment for 1 h at 800 °C followed by oxidation for 1 h in laboratory air, the coating developed a thin Cr_2O_3 thermally grown oxide (TGO), as confirmed by EDX and supported by XRD (Fig. 5b). Owing to the sharp and rough surface morphology, the oxide layer did not fully cover the surface continuously, although the columnar gaps were sealed by Cr_2O_3. An interdiffusion zone (IDZ) of about 3 μm was observed. EDX analysis revealed that Cr diffused into the alloy, while no elements from the substrate were detected within the coating. The coating adhered well to the alloy showing no cracks or spallation.

The Cr coating tested directly in laboratory air for 1 h after deposition also formed a Cr_2O_3 TGO, with oxidation occurring along the columnar gaps (Fig. 5c). In this case, no interdiffusion of Cr into the substrate was observed, but the coating continued to exhibit a well-adhered nature.

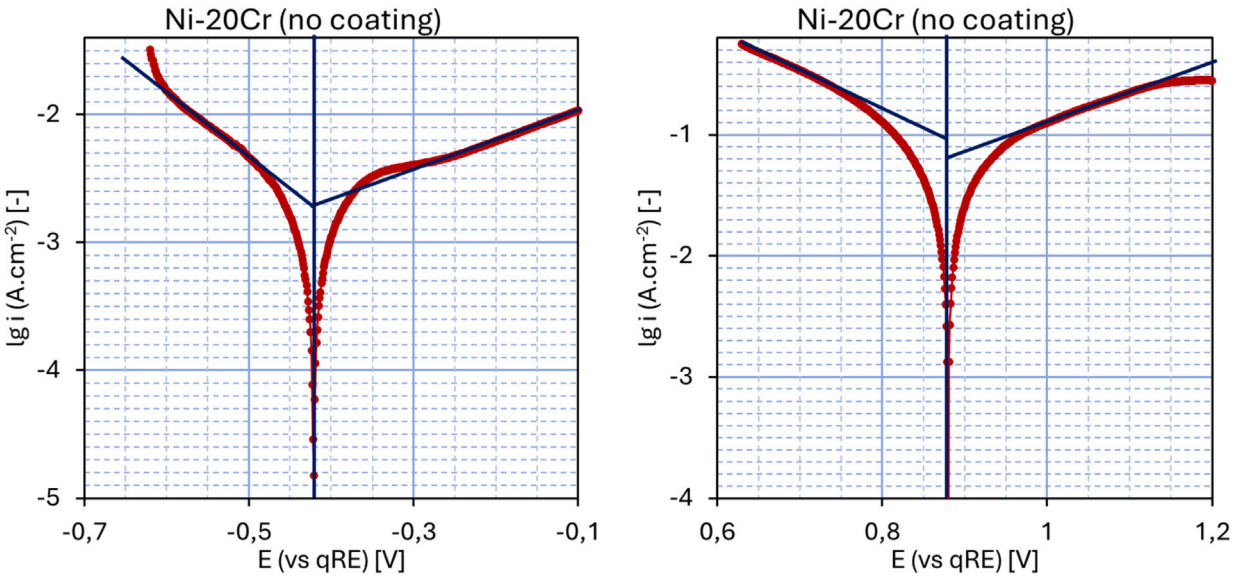


Fig. 2. Examples of a Tafel plot used to determine the exchange current density: left — after immersion, right — after 1 h-electrolysis at 0.1 A/cm_2.

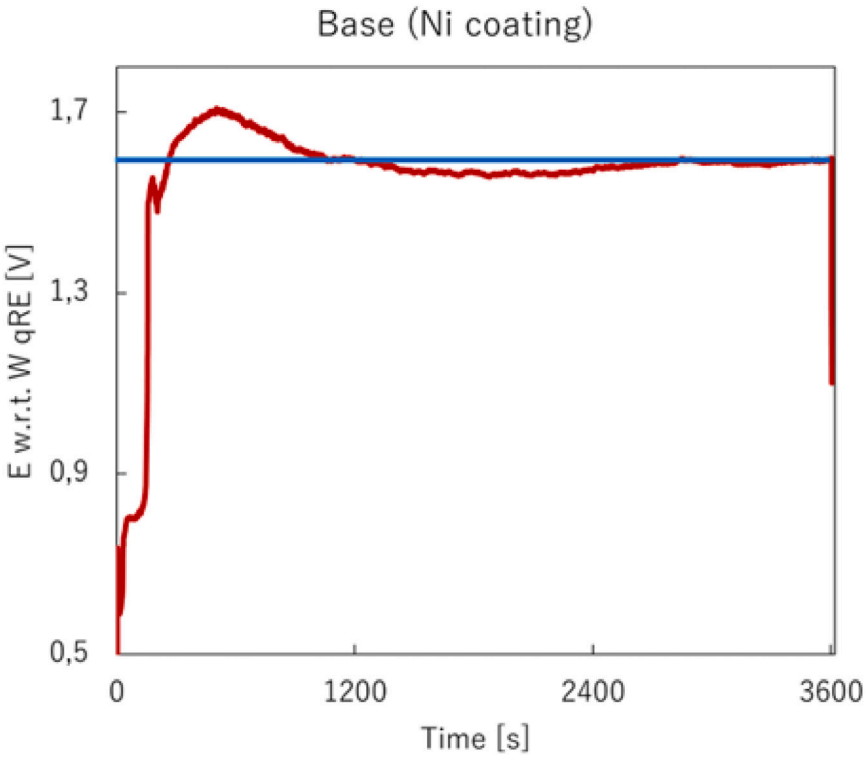


Fig. 3. Example of a chronopotentiometry plot used to determine the stationary potential.

The Ni–Cr20 coating develops wider columns than the pure Ni and Cr coatings. It adheres well to the alloy, exhibits a dense morphology, and is crystalline after deposition, with a thickness of about 11 μm, as shown in Fig. 6a.

After vacuum treatment for 1 h and subsequent oxidation in laboratory air at 800 °C for 1 h, the coating formed a continuous Cr_2O_3 thermally grown oxide (TGO), as shown in Fig. 6b. The columnar gaps were already closed during vacuum treatment. EDX analysis revealed that Cu and Fe diffused into the coating in amounts of approximately 9 at% each.

The Ni–Cr20 coating tested directly in laboratory air for 1 h after deposition also developed a Cr_2O_3 TGO. The columnar structure was still visible but closed off by the Cr-oxide formation, as shown in Fig. 6c. Fe and Cu were detected in the coating at about 5 at% each, while no interdiffusion was observed at the coating–alloy interface. The coating shows no cracks or spallation and therefore adheres well to the alloy under both conditions.

Since the oxidation behaviour of the vacuum-treated and the as-deposited samples tested for 1 h in ambient laboratory air showed very

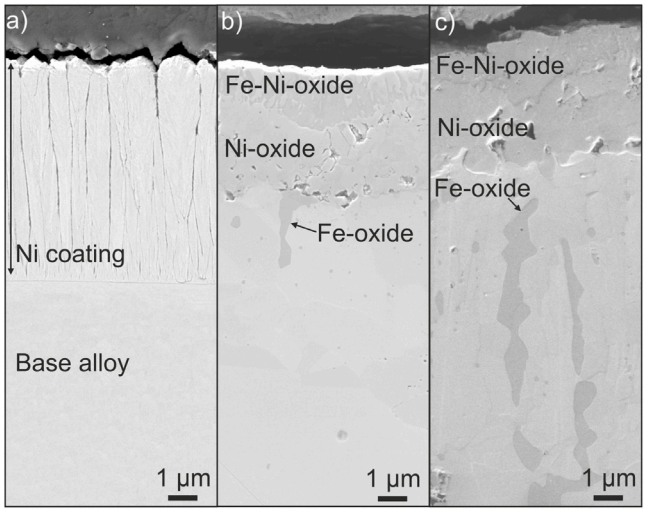


Fig. 4. SEM images of the Ni coating under different conditions: (a) as-deposited, (b) after 1 h vacuum + 1 h air treatment at 800 °C, and (c) after direct 1 h air exposure at 800 °C.

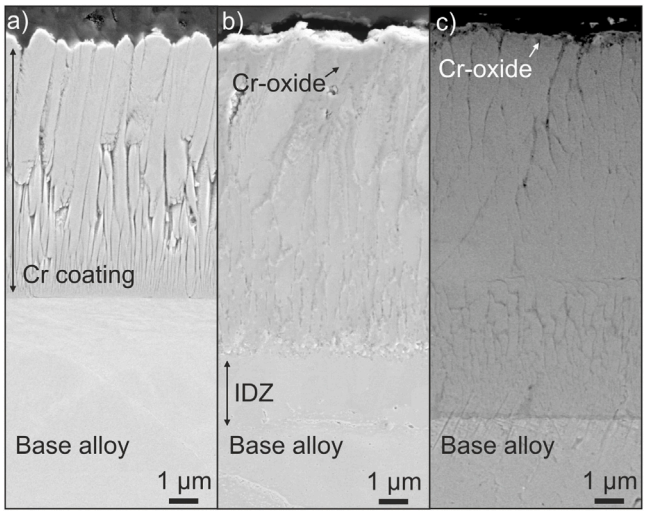


Fig. 5. SEM images of the Cr coating under different conditions: (a) as-deposited, (b) after vacuum + air treatment at 800 °C, and (c) after direct air exposure at 800 °C.

similar results, the as-deposited state in each case was selected for further use. This choice was made because maintaining the coatings in the as-deposited condition minimises interdiffusion, that occurred during vacuum annealing, and thus reduces the risk of adversely affecting the performance of the anodes.

3.2. Electrochemical measurements

3.2.1. Resistance towards fluoridation

The resistance of the anode towards metal dissolution or fluoridation was characterised by the exchange current density on the clean metal surface $i_{0(cl)}$ exposed to the melt. The resulting current densities and corresponding reversible potentials were plotted in Fig. 7a and b, respectively. The coated samples were tested directly after deposition with no additional air annealing

Exchange current density is a kinetic parameter that helps to assess the rate of the process, while the reversible potential is a thermodynamic property that can give a hint of what process is dominant.

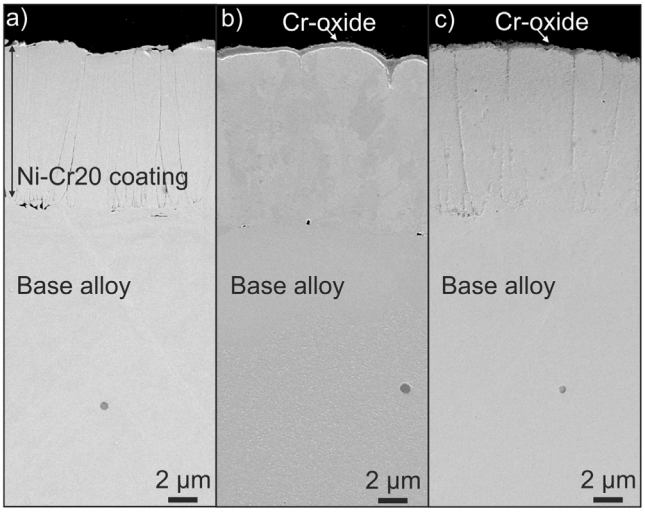


Fig. 6. SEM images of the Ni–Cr20 coating under different conditions: (a) as-deposited, (b) after vacuum + air treatment at 800 °C, and (c) after direct air exposure at 800 °C.

Judging by the reversible potentials one can say firstly, whether the coating remains on the surface or dissolves within the first minutes after the immersion, and secondly, whether the process on the coating is different compared to the process on the bulk anode of the same chemical composition. Exchange current densities were in the range from 0.1 to 8.0 mA/cm^2. On average, the presence of the coating did not affect the resistance towards fluoridation, except for the Ni–Cr20 coating, which made the fluoridation rate much higher. The sample with the bulk Ni–Cr20 composition did not demonstrate the same behaviour as the coating. In terms of the resistance towards fluoridation, the Cr coating did not show a considerable effect on the process, neither regarding the rate nor the nature of the process. The presence of the Ni coating did not affect the exchange current density; however, the corresponding reversible potential shifted towards more positive values. This serves as evidence that the coating affected the nature of the process, and this effect was caused not just by the nature of the Ni element but also by the properties of the coating itself. The evidence for that is that the average reversible potential of the bulk Ni sample was around 300 mV more negative. The average exchange current density on the clean bulk Ni anode was around 2 mA/cm^2 higher than that of the Ni-coated anode.

3.2.2. Resistance towards oxide dissolution

After performing the linear sweep voltammetry on the clean anode surface, the electrolysis at 0.1 A/cm^2 was performed for a duration of 1 h. The purpose of the electrolysis was firstly, to oxidise the surface of the anode and study the oxidation dynamics and secondly, to assess the resistance of the anode towards the electrical passivation. The current density was selected based on the assumption that, under the studied conditions, the anode will not be damaged and a smooth oxide scale deposition can be maintained. During the electrolysis, the potential difference between the anode and the quasi-reference electrode was recorded. After the electrolysis was finished and the initial oxide layer was formed, the linear sweep voltammetry was performed again, and the exchange current density on the oxidised surface was determined. The average values and corresponding average reversible potentials were plotted in Fig. 8a and b, respectively.

The values of exchange current density were in the range from 6.5 to 115.2 mA/cm^2, which is around 10 times higher than those on the clean surface. The corresponding reversible potentials were shifted around 1 V towards positive values. The exchange current densities presumably indirectly characterise the rate of oxide scale dissolution,

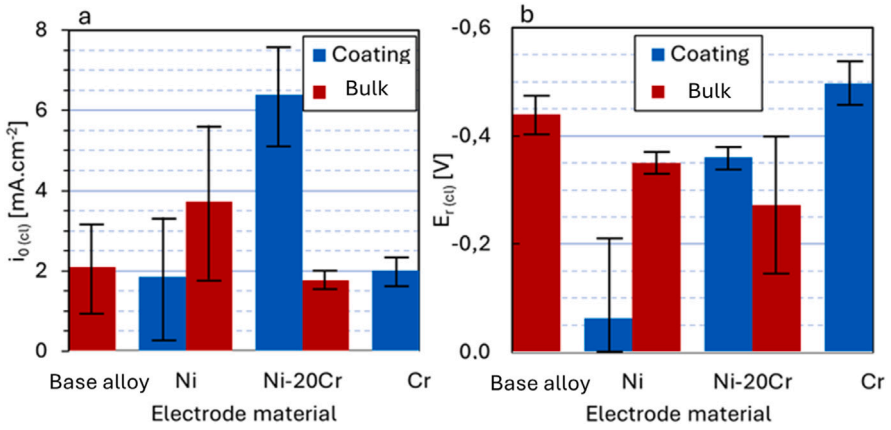


Fig. 7. The results of linear sweep voltammetry performed on a clean (non-oxidised) surface, with the blue bars representing the [Ni/Cr/Ni–Cr20 + $Ni_{42}Fe_{38}Cu_{20}$] material: a – average exchange current densities; b – average corresponding reversible potentials with respect to tungsten quasi-reference electrode (error bars represent the standard deviations of the three samples tested).

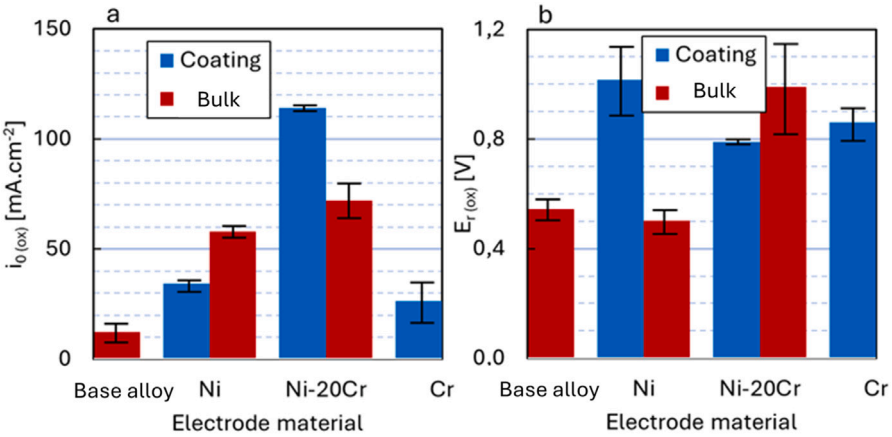


Fig. 8. The results of linear sweep voltammetry on an oxidised surface after 1-hour electrolysis at 0.1 A/cm^2 with the blue bars representing the [Ni/Cr/Ni–Cr20 + $Ni_{42}Fe_{38}Cu_{20}$] material: a – average exchange current densities; b – average corresponding reversible potentials with respect to tungsten quasi-reference electrode.

while the corresponding reversible potentials give an idea of the nature of the dominating dissolution process. The standard deviations of the exchange currents were considerably lower compared to those on the clean anodes. The lowest exchange current densities were demonstrated by the uncoated base samples. The Cr coating provided a slight increase in exchange currents, and the corresponding reversible potentials shifted towards more positive values. The Ni-coating demonstrated a considerable increase in exchange current density up to 33 mA/cm^2 on average compared to the uncoated base sample. The bulk Ni sample showed an even greater increase to 58 mA/cm^2. The reversible potentials of the Ni-coated anodes were also shifted towards more positive values. The same is true for the Ni–Cr20 coatings. This serves as evidence that the effect of the coatings remains after short-term polarisation. The average values were in a range from 0.8 to 1.0 V with respect to the quasi-reference electrode. The average reversible potential of the anode without a coating was 0.54 V. The highest values of the exchange current were demonstrated by the Ni–Cr20 coating, which is similar to what was observed when measuring the exchange current on clean anodes.

3.2.3. Resistance towards passivation and overall estimated wear rate

The potential–time plot recorded during the above-mentioned 1 h duration electrolysis was evaluated, and the stationary potential E_{st} was determined (Fig. 9a). Stationary potential provides the initial assessment of the resistance of the anode towards electrical passivation, and it also gives an idea of the ability of the anode to form a sustainable protective oxide scale. The normal values of the stationary potential are expected to lie in the range from 1.3 to 2.0 V with respect to the tungsten quasi-reference electrode. When the value is below this range, it means that the oxide scale cannot be formed or sustained, and the anode undergoes continuous metal dissolution. However, if the stationary potential is higher than the upper limit of the mentioned range or the stationary state is not reached, it means that there is a large portion of an electrically insulating compound. The wear rate was calculated according to Eq. (2) for each tested sample. Fig. 9c shows how a high wear rate does not necessarily correlate to thicker corrosion scale, suggesting either the scale constituents are more impactful, or in the case of the Ni–Cr20 coated samples for example, catastrophic breakaway corrosion is occurring during electrolysis.

The average values for each sample type were plotted in Fig. 9b. The average stationary potential of the base anode was 1.7 V with respect to the quasi-reference electrode. The application of the coatings did not change this value dramatically. For all coated [Ni/Cr/Ni–Cr20 + $Ni_{42}Fe_{38}Cu_{20}$ wt%] samples, the stationary potential was in the range from 1.62 to 1.80 V. For the pure Ni anode, the stationary potential was 0.78 V, demonstrating that a sustainable oxide scale cannot be formed on such an anode. The stationary potential of the bulk Ni–Cr20 anode was not reached in 2 out of 3 measurements, leading to a rise of the potential up to 5 V, which was a device limit. The wear rate calculated for the uncoated base sample was in the range from 0.46 to 1.40 g/m^2 h, which is the lowest among all tested samples. The Ni- and Cr-coated samples had a slightly higher wear rate, with average values of 1.31 and

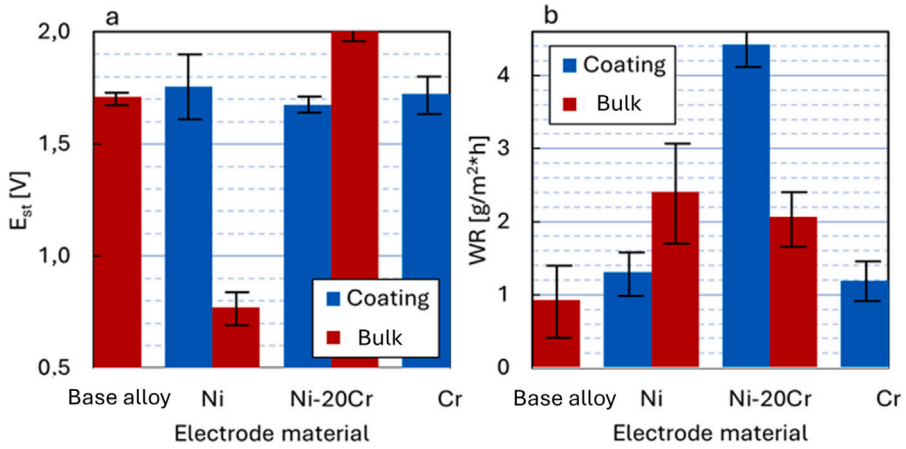


Fig. 9. Results of chronopotentiometry recorded during the 1 h-electrolysis at 0.1 A/cm^2 with the blue bars representing the [Ni/Cr/Ni–Cr20 + $Ni_{42}Fe_{38}Cu_{20}$] material (a) and calculated wear rates (b).

1.19 g/m^2 h, respectively. The worst performance was demonstrated by the Ni–Cr20 coating with the average wear rate of 4.40 g/m^2 h. The effect of the coating on the wear rate was not consistent among the tested compositions. The wear rate of the [Ni + $Ni_{42}Fe_{38}Cu_{20}$ wt%] coated anode is intermediate between the uncoated base anode and the pure Ni anode, while for the bulk Ni–Cr20 anode and the [Ni–Cr20 + $Ni_{42}Fe_{38}Cu_{20}$ wt%] anode, the tendency is different. The [Ni–Cr20 + $Ni_{42}Fe_{38}Cu_{20}$ wt%] anode has an average wear rate that is considerably higher than both the uncoated base anode and the Ni–Cr20 bulk anode.

Fig. 10(a) shows how the corrosion current densities on the oxidised anode surface and clean anode surface evolves as the scale thickness increases. At a thickness of 289 μm the average rate of metal dissolution is reduced to its lowest value at 1.50 mA/cm^2 whilst the average rate of oxide dissolution rises to its highest value at 66.8 mA/cm^2. The mean corrosion current density values demonstrate a trend of increasing oxide dissolution rate and decreasing metal dissolution rate as scale thickness increases, although large variability prevents the emergence of a clear statistical separation. Fig. 10(b) demonstrates an increase in the mean wear-rate up to 147 μm and a slight decrease as the scale thickness is approximately doubled at 289 μm with a similarly large wear rate variability preventing a clear statistical pattern from emerging.

Even though the studied coatings did not enhance the performance of the base anode, they noticeably affected the electrochemical behaviour not just in terms of the chemical nature of the elements that constitute the coating, but also the structural properties of the coatings. The electrochemical measurements demonstrated that the effect of the coating remains even after 1 h of electrochemical oxidation. The SEM & EDX analyses were performed to shed light on the reasons behind the differences in the electrochemical parameters.

3.3. SEM & EDX analysis of corrosion scales

Fig. 11 shows the typical morphologies of the coated and uncoated alloys after electrolysis at low magnifications. The different anode types were observed to produce a *somewhat* similar corrosion scale morphology to one another. The uncoated $Ni_{42}Fe_{38}Cu_{20}$ wt% anodes in particular seem to exhibit a scale prone to blistering with relatively poor adhesion to the bulk. Extensive blistering and spalling of the scale was also observed in 2/3 of the investigated regions for the [Ni–Cr20 + $Ni_{42}Fe_{38}Cu_{20}$] coated anodes. The most notable characteristic observed in the uncoated base anode cross-sections was the much greater penetration of the electrolyte into the bulk as seen in Figs. 11 and 12. The average scale thickness and electrolyte penetration depth across all anode-types is displayed in Table 3. Each of the coatings is seen to inhibit the penetration of the electrolyte beneath the scale to varying extents, with Ni exhibiting the smallest electrolyte penetration zone. Fig. 12 shows a depletion of constituent Ni, Fe and Cu in the bulk inside the electrolyte penetration zone, indicative of a more prominent metal dissolution of bulk constituents. Cr-coated alloys were observed to have the thinnest corrosion scales (Table 3) that possess a morphology with minimal blistering and good overall adhesion to the bulk material (Fig. 12).

Table 3
Corrosion scale thickness and electrolyte penetration depth averaged across all samples.

Base alloy composition wt%	Coating	Avg. scale thickness (μm)	Avg. electrolyte penetration (μm)
$Ni_{42}Fe_{38}Cu_{20}$	Ni	113.01	35.00
$Ni_{42}Fe_{38}Cu_{20}$	Cr	46.73	41.28
$Ni_{42}Fe_{38}Cu_{20}$	Ni–Cr20	85.95	37.02
$Ni_{42}Fe_{38}Cu_{20}$	None	164.19	90.84

EDX analysis revealed that, despite the differences in scale thickness and structure that appear to arise due to the coating conditions, the chemical composition of the corrosion scales retains similarities. An outer-layer rich in electrolyte species (Al, F, Na, K) consistently forms. The oxide layer containing constituent elements from the bulk and the coating (Ni, Fe, Cu, Cr, O) usually forms at the interior of the scale, although Fig. 12 shows how blistering events may cause irregularities in this typical layer structure. Cu was observed only in very weak quantities regardless of the coating type, suggesting none of the coatings is able to prevent the outward diffusion of Cu into the electrolyte. Fig. 12 also shows how the measured Cr-coated anode gives rise to a uniform oxide layer richest in Fe with some Ni, which is a strong indicator of the formation of a (Ni, Fe)O spinel structure. Cr was observed in weak quantities within the oxide scale in small localised regions, suggesting the majority of the coating dissolved during operation. In contrast, the oxide layer of the uncoated base-alloy is shown to possess a more incoherent structure that is Fe-rich and Ni-poor, suggesting an oxide layer consisting of mainly Fe-based products (FeO, Fe_2O_3, Fe_3O_4) within this region, as well as (Ni, Fe)O spinel oxides.

EDX mappings of both the Ni and Ni–Cr20 coated anodes (Fig. 13) were observed to influence the chemical composition of the corrosion scale moreso than the Cr-coated anodes. In both cases a greater Ni content was observed in the corrosion scale in comparison to the uncoated anodes. For the Ni coated anodes, the Ni-rich regions overlapped with Fe and O suggesting the formation of a spinel (Ni,Fe)O oxide similar to the Cr-coated anodes. Ni–Cr20 coated anodes also show evidence of a (Ni,Fe)O spinel oxide phase, as well as more prominent overlapping of Ni and F regions indicating the presence of NiF_2.

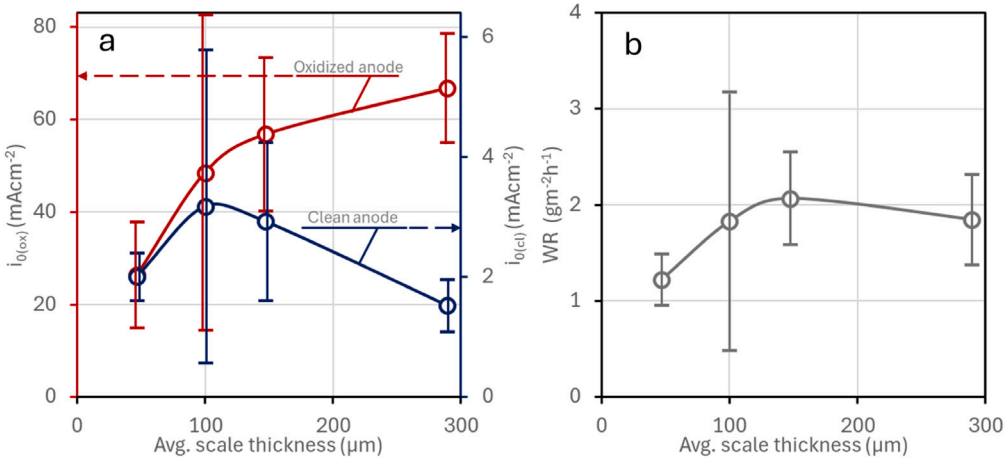


Fig. 10. (a) Average oxidised anode (red, left y-axis) and clean anode (blue, right y-axis) corrosion current densities, plotted as a function of average corrosion scale thickness. (b) Average wear rate plotted as a function of average corrosion scale thickness.

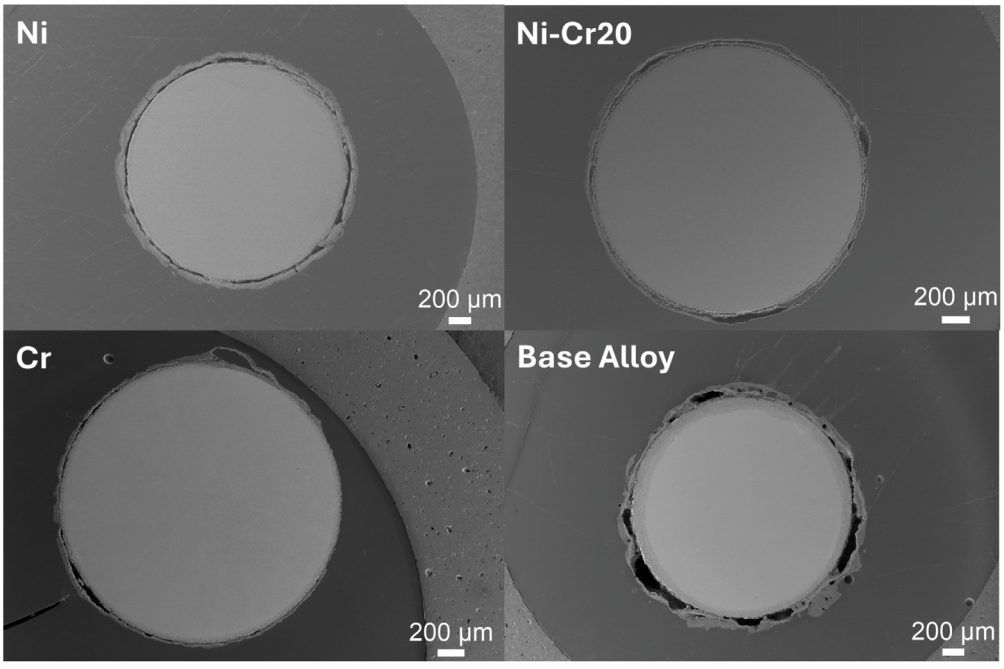


Fig. 11. Low magnification SEM images of anode cross-sections for the Ni, Ni–Cr20 and Cr coated anodes as well as the uncoated base anode after electrochemical measurements and 1 h of electrolysis at T = 800 °C.

Greater Cr concentration was observed in the Ni–Cr20 coated anodes in the corrosion scale/oxide region and sub-scale penetration zone compared to their Cr-coated counterparts, potentially indicative of Cr_2O_3, (Ni,Cr)O, (Fe,Cr)O formation and suggesting Cr diffusion and dissolution is inhibited in the mixed Ni–Cr20 coating. Both the Ni and Ni–Cr20 coated anodes lead to a reduced electrolyte penetration compared to Cr-coated anodes (Table 3) at the expense of a much thicker corrosion scale. Whilst Fig. 9 suggests there being no improvement in wear-rate for Cr- and Ni-coated anodes vs. their uncoated counterparts, the SEM and EDX findings suggest an overall (scale thickness + electrolyte penetration) reduced attack of the electrolyte and the formation of a more uniform oxide structure that *does* imply improved corrosion behaviour.

Fig. 13 shows the corrosion structure that is typically formed in the [Ni + $Ni_{42}Fe_{38}Cu_{20}$] coated anodes as well as the tendency of the [Ni–Cr20 + $Ni_{42}Fe_{38}Cu_{20}$] coated anodes to blister and adhere poorly to the bulk. The relatively thin electrolyte penetration zone can be observed underneath the scale, as well as the tendency of the blisters to alter the relative position of the oxide layer. Blistering of the scale during oxidation allows for irregular electrolyte penetration between the oxide layer and bulk, causing the oxide layer to appear non-uniform over a given time period. The two out of three Ni–Cr20 coated anodes that exhibit extensive blistering are the two samples that also exhibit the highest wear-rate measurements in Fig. 9, likely due to the formation of the passivating NiF_2 compound, that was seemingly not as prevalent in both the Ni and Cr-coated anodes.

Fig. 14 shows the corrosion scale structure for both the pure Ni and bulk Ni–Cr20 anodes, exposed to identical electrolysis conditions as the [Ni/Cr/Ni–Cr20 + $Ni_{42}Fe_{38}Cu_{20}$ wt%] coated anodes. Both exhibit a large variance in their corrosion scale thickness, suggestive of a non-uniform response of the corrosion mechanism across samples. For the bulk Ni–Cr20 anode #1 sample, extreme blistering and spalling is observed with an average scale thickness of 422.94 μm which was the largest of all analysed cross-sections. The corrosion scale thickness of the bulk Ni–Cr20 anode #2 was measured to average out at 121.57 μm, with a large variance around its perimeter. Between each bulk Ni–Cr20

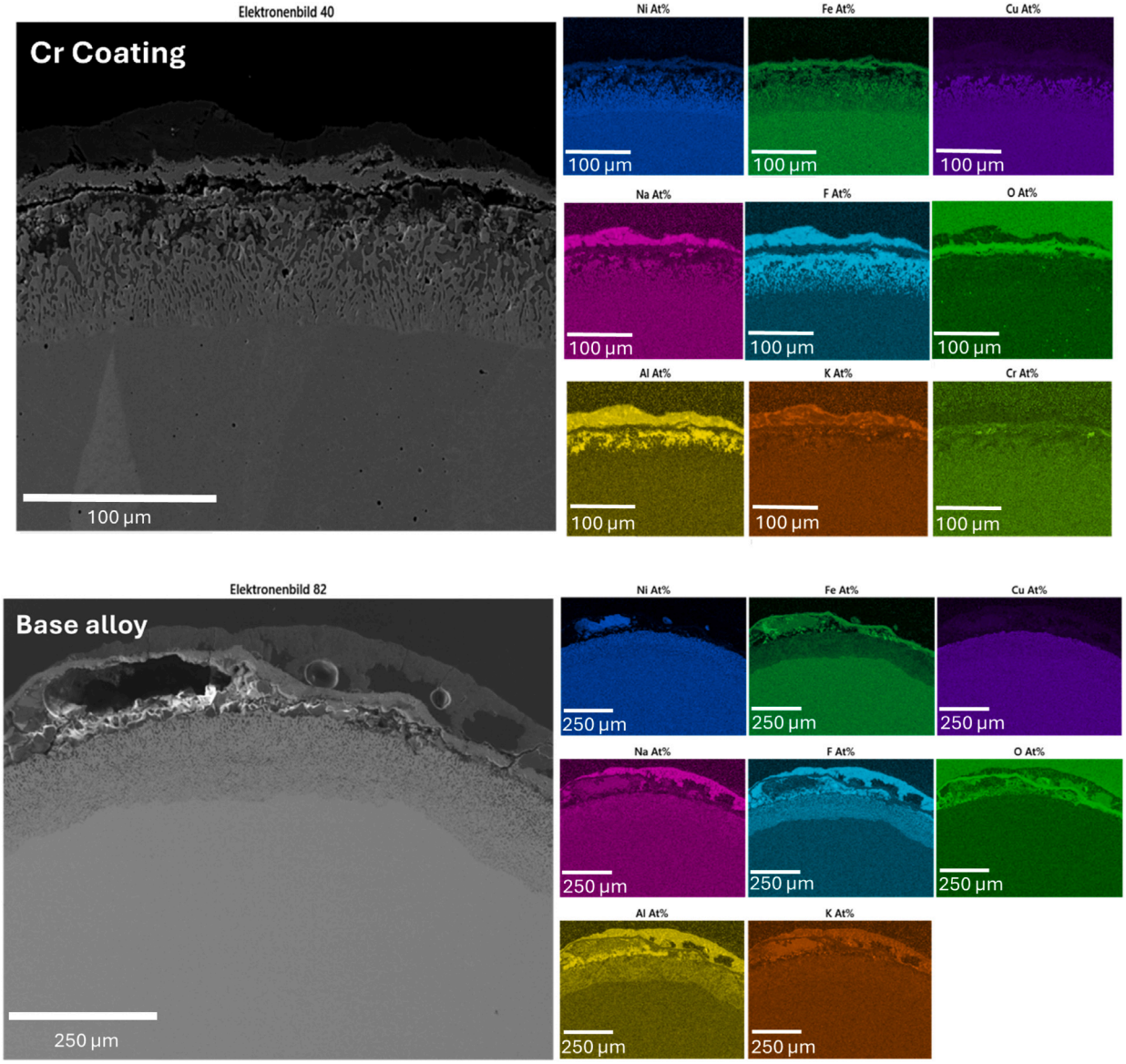


Fig. 12. EDX mappings of Cr-coated and base anode cross-sections after 1 h of electrochemical measurements at 800 °C.

anode, it is inconclusive as to whether the large difference in average corrosion scale thickness is due to the delamination of the scale during electrolysis or due to an intrinsic variance in the corrosion mechanism. The scale structure observed for bulk Ni–Cr20 anode #1 in Fig. 14 shows a scale with many cracks and empty blisters – supporting the notion that catastrophic breakaway corrosion in bulk Ni–Cr20 anode #2 and a thinner resultant scale gives the illusion of a reduced electrolyte attack and improved performance. Of the coated anodes, Ni–Cr20 samples were also observed to be the most prone to blistering, which would suggest this material possesses an inability to reliably form a compact, adherent and suitably protective corrosion scale within these electrochemical conditions. With respect to the pure Ni anodes, a similar comparison can be made, albeit with a reduced effect. A large variance in average scale thickness is observed with 244.19 µm for Ni anode #2 compared to 139.67 µm for Ni anode #1. Electrolysis of the pure Ni anodes lead to the formation of a more compact and dense scale with a more irregular morphology, a behaviour which is weakly mimicked by their [Ni + $Ni_{42}Fe_{38}Cu_{20}$] counterparts, and more strongly mimicked in [Ni–Cr20 + $Ni_{42}Fe_{38}Cu_{20}$] anodes. The highly Ni-rich material selection for the pure Ni and bulk Ni–Cr20 anodes is likely inducing extensive NiF_2 formation, passivating the anode and causing irregular current density distributions that lead to the irregular corrosion scale formation observed in Fig. 14.

4. Discussion

4.1. Coating of alloys oxidation resistance

The microstructural evolution of the coatings can be interpreted using the Thornton structure zone model (SZM). This model describes sputtered film morphologies as a function of the homologous temperature (T/T_m, calculated in Kelvin) and working pressure during deposition [22]. For Ni (T_m = 1455 °C [23]) and Cr (T_m = 1840 °C [24]), the effective deposition temperatures were T_{Cr} = 143 °C, T_{Ni} = 208 °C, and $T_{Ni–Cr20}$ = 242 °C. At these relatively low homologous temperatures and under a working pressure of 0.47 Pa, the coatings fall within Zone *T* of the Thornton SZM, which is characterised by dense columnar grains with straight boundaries [22]. This is consistent with the fine, well-defined columnar structures observed in the Ni coating, Fig. 4a. The Cr coating also displayed columnar growth but with bending of the columns at one-third of the thickness (Fig. 5a). Such behaviour is most likely related to the cylindrical sample geometry and associated

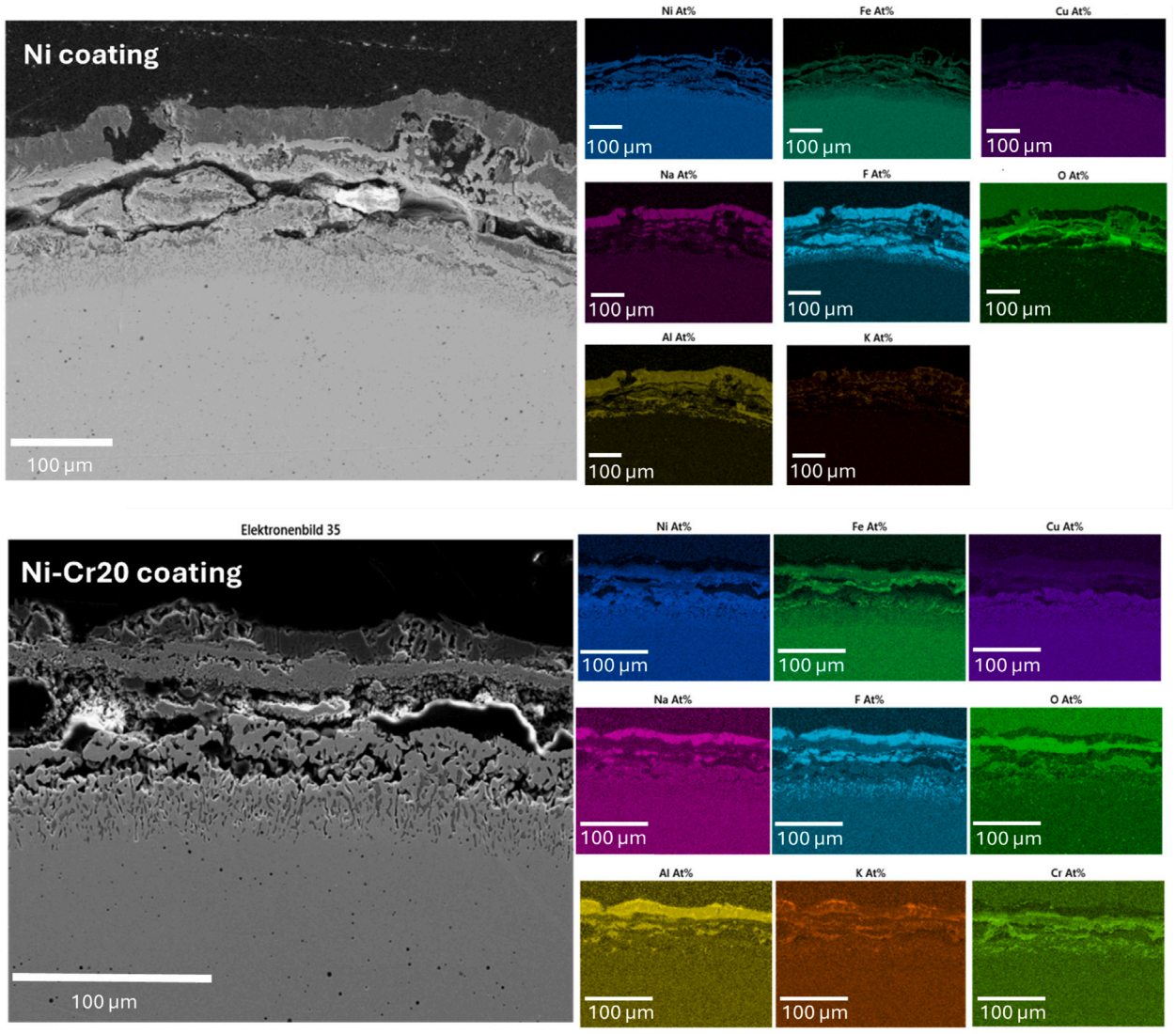


Fig. 13. EDX mappings of Ni and Ni–Cr20 coated anode cross-sections after 1 h of operation at 800 °C.

shadowing or rotation effects during deposition [25]. The Ni–Cr20 coating exhibited wider columns, which can be attributed to co-sputtering of two elements and associated changes in atom mobility (Fig. 6a). Nevertheless, this coating also corresponds to Zone T.

The samples were oxidised at 800 °C for 1 h, both with and without a prior vacuum-annealing step at the same temperature. After heat treatment at 800 °C, significant differences in diffusion and oxidation behaviour were evident among the three coatings. Fig. 4b shows that the Ni coating underwent rapid interdiffusion with the substrate, resulting in the disappearance of its columnar morphology and the formation of a mixed interface. Fe and Cu diffused into the coating, while Ni diffused into the substrate. A two-layered thermally grown oxide (TGO) developed, consisting of an outer Fe–Ni-rich oxide and an inner NiO-rich layer. This oxidation mechanism is consistent with outward Fe diffusion and inward Ni oxidation, and is comparable to the oxidation of the uncoated Ni–Fe–Cu alloy [26]. The coating in Fig. 4c shows similar behaviour. Internal oxidation is more prevalent due to the intercolumnar gaps. Since no vacuum treatment was performed, the columns closed off by oxidation, causing deeper penetration of oxygen inside the coating. These findings confirm that pure Ni does not provide an effective diffusion barrier under these conditions.

The Cr coating behaved differently. After exposure at 800 °C for 1 h, vacuum treatment followed by air oxidation, a thin but protective Cr_2O_3 scale formed on the surface. Although the oxide was not fully continuous due to the rough surface morphology, the columnar gaps were sealed by Cr_2O_3, which contributed to its protective properties. The relatively small oxide thickness may be explained by the short testing time. An interdiffusion zone (approximately 3 µm) formed at the coating–substrate interface. Cr diffused into the substrate, but no substrate elements were detected in the coating, Fig. 5b. This behaviour reflects the well-established protective role of Cr_2O_3 as a TGO in high-temperature environments [27]. Coatings without vacuum treatment exhibited similar behaviour, although no IDZ could be observed, Fig. 4c.

The Ni–Cr20 coating exhibited intermediate behaviour, combining features of both pure coatings. A continuous Cr_2O_3 scale formed, which effectively sealed the columnar gaps. This result was expected given that Cr has a higher affinity for oxygen and greater thermodynamic stability than Ni [28,29]. Similar findings have been reported in other studies of Ni–Cr20 coatings, in which $NiCr_2O_4$ spinel and NiO were also identified, in addition to Cr_2O_3 [29,30]. In the present study, however, only Cr_2O_3 was observed, Fig. 6b. Unlike the pure Ni coating, the Ni–Cr20 coating suppressed interdiffusion at the coating–substrate interface. This confirms that even moderate Cr additions can stabilise oxide formation and enhance barrier performance. Nevertheless, EDX detected Cu and Fe within the coating at levels of 5–9 at%, indicating that diffusion still occurred to some extent, albeit less than in pure Ni. The diffusion behaviour observed here is consistent with the findings of

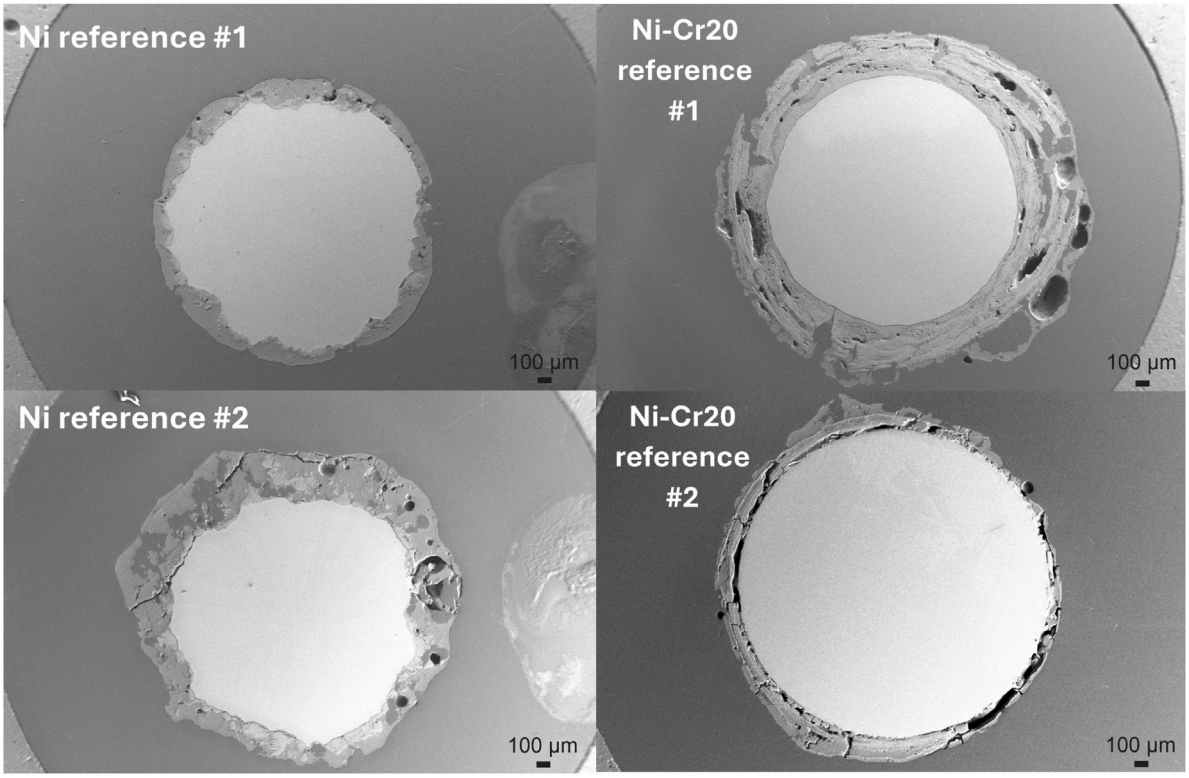


Fig. 14. SEM cross-sections of two pure Ni and bulk Ni–Cr20 anodes after 1 h of operation in electrolysis at 800 °C.

Jalilvand et al. [29]. The coating in Fig. 6c without vacuum treatment shows columnar gaps with minor oxide formation. The coating itself exhibits interdiffusion and sealing due to the formation of a closed TGO.

Overall, the results demonstrate the strong influence of coating composition on high-temperature performance. The Ni coating offered only short-term protection and was prone to rapid interdiffusion and non-protective oxide formation. In contrast, the Cr and Ni–Cr20 coatings showed significantly better oxidation resistance, with adherent and protective Cr_2O_3 scales. These findings underscore the importance of Cr in stabilizing protective oxide layers and highlight the Ni–Cr20 composition as a promising compromise between structural compatibility and oxidation resistance.

4.2. Corrosion behaviour

4.2.1. Metal dissolution

The electrochemical activity of the unoxidised substrate is characterised by the apparent exchange current density ($i_{0(cl)}$) which serves as a kinetic proxy for the metal fluoridation reaction that can be generalised as $M + nF^- \rightarrow MF_n + ne^-$, where M represents Ni, Fe, Cu or Cr constituents reacting with fluoride species (F^- or AlF_x). The electrochemical measurements suggest a lack of improvement in corrosion resistance compared to the base alloy, for all three coating types. Fig. 7 shows that both Ni and Cr-coated anodes cannot be said to have behaved significantly differently than the base alloy with respect to metal dissolution/fluoridation. The rapid interdiffusion observed for the Ni-coating with substrate elements likely means the [Ni + $Ni_{42}Fe_{38}Cu_{20}$] surface exposed to the electrolyte is similar in composition to the uncoated $Ni_{42}Fe_{38}Cu_{20}$ alloy, which correlates with the similar dissolution behaviour observed between the two. For the Cr-coated anodes, whilst the observed interdiffusion was less extensive compared to the Ni-coated anodes, exposure to the molten electrolyte likely caused the rapid fluoridation of the Cr coating from, as evidenced by the weak Cr presence in Fig. 5, due to the greater thermodynamic drive for fluoridation of Cr compared to Ni [31]. Rapid Cr dissolution upon initial contact with the electrolyte, leaving behind only a weakly Cr-enriched surface, would then explain the similar kinetics characteristics between [Cr + $Ni_{42}Fe_{38}Cu_{20}$] and $Ni_{42}Fe_{38}Cu_{20}$ anodes observed in Fig. 7.

Comparing pure Ni anodes with their [Ni + $Ni_{42}Fe_{38}Cu_{20}$] counterparts, the fluoridation kinetics are broadly comparable, as reflected by the overlapping exchange current density ($i_{0(cl)}$) values. The lower average $i_{0(cl)}$ observed for the [Ni + $Ni_{42}Fe_{38}Cu_{20}$] coated anodes likely arises from the anode surface behaving similarly to an uncoated ternary Ni–Fe–Cu alloy. The higher driving force of fluoridation for Fe promotes its preferential corrosion and segregation from the bulk, resulting in the development of a Ni–Cu-enriched region beneath the corrosion scale. The formation of a Ni–Cu-rich depletion zone, with a Cu content exceeding that of the bulk alloy, is expected to reduce the local electrochemical activity towards fluorine. In addition, continued fluoridation of Fe is increasingly limited by diffusion from the bulk through this depletion zone. Together, these effects provide a plausible explanation for the lower average exchange current densities observed for both the uncoated base alloy and the Ni-coated anodes.

The relationship between initial electrochemical activity and scale thickness reveals a transition in behaviour at > 100 µm (Fig. 10a). Up to a thickness of approximately 100 µm, increased kinetics on the clean surface ($i_{0(cl)}$) and oxidised surface ($i_{0(ox)}$) correlates with increased scale growth and subsequent wear rate as defined by Eq. (2). This positive correlation expectedly increases for $i_{0(ox)}$. At > 100 µm scale thickness a decrease in the clean surface kinetics is observed. This indicates that the reduced metal dissolution kinetics prior to oxygen evolution do not necessarily translate to a more protective substrate, as the anodes with the thickest average corrosion scales (bulk Ni–Cr20 and Ni) form insulating compounds such as NiF_2 which lead to cell passivation and an increase in the kinetics on the oxidised anode surface.

The Ni–Cr20 coating was observed to have a much greater (albeit negative) impact with a measured increase in the electrochemical activity compared to the base alloy. Upon exposure to the bath, the

greater driving force of fluoridation for Cr would cause its preferential corrosion and segregation from the Ni–Cr20 matrix, leaving behind a Cr-depleted and Ni-rich layer. The dealloying caused by Cr segregation has been observed to increase porosity of the Ni-rich region underneath, which would lend itself to greater infiltration from the electrolyte as well as enhancing dissolution of the coating via a galvanic coupling effect [32,33]. This effect appears to be mitigated in the bulk Ni–Cr20 anode, where the homogeneous distribution of Cr enables continuous replenishment of Cr at the anode surface via diffusion from the bulk, thereby limiting the formation of a severely Cr-depleted, porous Ni-rich sub-layer.

4.2.2. Oxide dissolution

The kinetics of oxide scale dissolution is characterised by $i_{0(ox)}$, encompassing both direct oxide dissolution (as per Eq. (1)) and electrolyte penetration and subsequent metal fluoridation on the oxidised surface of the anode during electrolysis [17].

The base composition is known to produce a thick, well-adhered and relatively insoluble $NiFe_2O_4$ layer during oxidation [26]. In general, the coatings worsened the measured electrochemical activity of the oxidised anode surfaces ($i_{0(ox)}$) in each case, with the worst-performer Ni–Cr20, causing an approximate ten-fold increase in the apparent exchange current density on their oxidised surface compared to the base alloy. Fig. 6b shows how these coated anodes tend to oxidise with a Cr_2O_3 layer across the perimeter of the grains, with no NiO. During electrolysis this Cr_2O_3 layer is formed during oxygen evolution on the anodes surface, where F^- and AlF_x species facilitate the subsequent dissolution of this Cr_2O_3 layer through the formation of soluble oxyfluoride Cr complexes [34]. Thin and soluble Cr_2O_3 formations would then be prone to a higher frequency of electrolyte penetration, where the aggressive fluoride species can come into contact with the metal anode surface [17] giving rise to more extensive anode dissolution. Consequently, due to the minimal interdiffusion of substrate elements into the coating, a highly Ni-rich environment is then exposed to the electrolyte as the finite Cr coating is depleted, becoming subject to significant fluoridation from F^- and AlF_x species. Extensive blistering of the scale occurred in 2/3 of the [Ni–Cr20 + $Ni_{42}Fe_{38}Cu_{20}$] coated anodes, with EDX mappings (Fig. 13) suggesting the presence of a relatively high amount of NiF_2 resulting from Ni fluoridation. For the [Ni–Cr20 + $Ni_{42}Fe_{38}Cu_{20}$] anodes it is probable that the high Ni-content lends itself to extensive NiO formation during electrolysis [35] (with the thin Cr_2O_3 rapidly dissolving) which then evolves to NiF_2 via nickel fluoridation, passivating the cell and causing extensive corrosion where passivation in this context refers to the formation of NiF_2, an electrical insulator. While this layer inhibits the intended electrochemical reaction, it leads to localised cell polarisation and high over-potentials, which physically destabilise the scale and cause the observed blistering. For the bulk Ni–Cr20 anode, the consistent diffusion of Cr from the bulk to the surface likely somewhat inhibits the formation of NiO in favour of Cr_2O_3, limiting this passivation effect. The lack of Fe also means the relatively insoluble (Ni, Fe)O cannot form and reduce the rate of anodic consumption.

The Ni-coated anodes seem to avoid this passivation behaviour due to substantial interdiffusion between the coating and substrate elements, allowing for the formation of less detrimental (Ni,Fe)O and Fe-oxides, leading to a corrosion mechanism comparable to that of a Ni–Fe–Cu surface where a more protective oxide can form. For the pure Ni anode, a stable oxide was not formed and passivation via NiF_2 formation occurred. The lower electrochemical activity of the oxide for the Ni anode compared to the bulk Ni–Cr20 anode can be explained via the absence of the more reactive Cr and a galvanic coupling effect potentially accelerating anodic consumption. Fig. 8 demonstrates how the Cr-coating, with an average $i_{0(ox)}$ still higher than the uncoated base composition, had the lowest measured electrochemical activity across all coated samples. A thin Cr_2O_3 layer likely forms during the initial stages of electrolysis where it is subject to dissolution from F^- and AlF_x (Fig. 5b), with the diffusion of Cr into the substrate likely affecting the corrosion mechanism after the dissolution of the Cr_2O_3 layer due to the high oxygen affinity of Cr. A key perceived benefit of the Cr-coating versus the Ni and Ni–Cr20 coatings, is that it does not enrich the anode surface with Ni, limiting the NiO → NiF_2 corrosion pathway. The slight increase in the Cr-coated $i_{0(ox)}$ observed versus the base alloy may be explained by Cr presence in the substrate-alloy interface interfering with the oxidation mechanism that allows for $NiFe_2O_4$ formation. Both NiO and Fe_2O_3 formation is likely inhibited by the Cr present due to its high oxygen-affinity. Both of these oxides are prerequisites for the spinel (Ni,Fe)O forms [19,26,36]. The formation of Cr_2O_3 would therefore be prioritised in locally rich Cr regions, and the resultant scale would then demonstrate an increase in the apparent exchange current density $i_{0(ox)}$ and a greater anodic consumption rate relative to the more insoluble (Ni,Fe)O scale of the uncoated anodes.

Ultimately, the roles of the fluoride species such as F^- and AlF_x in oxide dissolution facilitates both the flux of metal Ni, Fe, Cu and Cr ions into the bath via direct scale/metal dissolution, as well as forming insulating NiF_2 phases in Ni-rich environments that may lead to anode failure. The tendency of all the coatings to produce other more soluble oxide products instead of $NiFe_2O_4$ during initial electrolysis and oxygen evolution, provides an explanation for the base-alloy ultimately possessing the lowest calculated wear rate as per Eq. (2) (Fig. 9) over the duration of the measurements.

4.2.3. Wear rate & scale morphology

Despite this, SEM and EDX analysis of the corrosion scales demonstrates a change in scale morphology as well as electrolyte penetration depth across each anode archetype. Comparing the corrosion scale of the Cr-coated anodes, which possessed the lowest calculated wear-rate (Eq. (2)) of the coated variants, to the uncoated anodes with the lowest overall calculated wear rate - on average the Cr-coated anodes possess a thinner corrosion scale, less extensive blistering and a reduced electrolyte penetration depth into the bulk (Fig. 5, Table 3). While the appearance of a thin, well-adhered scale might suggest material loss during electrolysis, the reduced penetration of the electrolyte into the anode substrate (Table 3) supports the hypothesis that the Cr-coating provides superior bulk protection. It is proposed that initial Cr_2O_3 formation acts as a sacrificial barrier, providing a period of protection to the substrate underneath to form $NiFe_2O_4$ - similar to the role of external Cu oxidation in facilitating the formation of $NiFe_2O_4$ [19,26,36] on the surface of regular Ni–Fe–Cu anodes. The initial formation and dissolution of a Cr_2O_3 barrier into the bath (via the formation of soluble Cr complexes) would explain the increased kinetics on the oxidised surface of the Cr-coated anodes measured in Fig. 8, as well as the near absence of the Cr in EDX mappings (Fig. 5). Consequently, this would mean the Cr-coating is effective in providing some short-term protection for up to 1 h in these electrolysis conditions. A similar albeit weaker behaviour is demonstrated by the [Ni + $Ni_{42}Fe_{38}Cu_{20}$] anodes.

The increase in measured electrochemical parameters (correlating to poorer corrosion resistance) in Cr and Ni coated anodes can then be linked to the accelerated dissolution of the *coating* material rather than the *substrate* material, with the substrate being partially insulated from fluoridation, as evidenced by the reduced penetration of the molten electrolyte (Table 3). The Cr and Ni coated anodes leaving behind a more compact corrosion scale may also mean that the calculated wear rate over electrolysis runs beyond 1 h *could* be lower than that of the uncoated base alloy, although this cannot be stated with certainty based off of the measurements presented in this study. Overall, elemental Cr and Ni coatings can be said to provide short-term protection to the anode in these electrolysis conditions.

The corrosion mechanism of Ni–Cr20 coatings on average, while also able to insulate the bulk from attack by the molten electrolyte and fluoridation in a similar manner (Table 3), greatly enhances passivation and cannot be said to provide any short-term benefit to the anode.

Taken together with the findings of Jalilvand et al. [21], which reports delamination of [Ni–Cr + (Co,Ni)O] coatings during electrolysis for Ni-rich and Cu-rich ternary alloys, the present results strongly indicate that Ni–Cr20 is not a suitable coating material for Ni–Fe–Cu anodes and may be limited to strictly boosting corrosion resistance in dry oxidising environments such as air and O_2, in which the [Ni–Cr20 + $Ni_{42}Fe_{38}Cu_{20}$] anodes showed promise.

Overall, [Cr + $Ni_{42}Fe_{38}Cu_{20}$] anodes possess slightly better electrochemical parameters than their [Ni + $Ni_{42}Fe_{38}Cu_{20}$] counterparts, with an average calculated wear rate of 1.19 g/m^2 h vs. 1.31 g/m^2 h respectively. In addition, when also considering the improved corrosion scale uniformity and adhesion observed in the Cr-coated anodes, it can be concluded that the Cr-coating was the strongest performer of the Cr/Ni/Ni–Cr20 coating types, followed closely by the Ni-coating. The Cr/Ni coating layers were observed to partially insulate the underlying $Ni_{42}Fe_{38}Cu_{20}$ substrate material from corrosion during the initial stages of electrolyte exposure, potentially allowing time for favourable (Ni, Fe)O spinel formation underneath. Future studies should seek to prolong the coating layer lifespan through the selection of a more insoluble coating constituent and through the potential application of pre-oxidation treatments on [coating + alloy] anodes.

5. Conclusion

The viability of Ni, Cr and Ni–Cr20 as coatings to improve the corrosion resistance of $Ni_{42}Fe_{38}Cu_{20}$ wt% oxygen-evolving anodes for aluminium electrolysis was investigated. Each coating demonstrated good adhesion to the bulk. Extensive interdiffusion between the coating and substrate was observed for the Ni-coating, leading to an oxidation behaviour that mimics regular Ni–Fe–Cu compositions with an enhanced Ni:Fe ratio and demonstrates the inefficacy of pure Ni to act as a diffusion barrier at elevated temperatures. For both the Cr and Ni–Cr20 coating, interdiffusion was found to be greatly reduced by the presence of a Cr_2O_3 oxide layer across the grain boundaries, consistent with established literature.

Electrochemical measurements concluded that the apparent exchange current densities ($i_{0(cl)}$,$i_{0(ox)}$) and the resulting calculated wear rates (WR) were, on average, higher in the Cr and Ni-coated anodes compared to the base alloy after 1 h of operation. However, SEM analysis does show a more compact corrosion scale forming for both of these coating types, along with a reduced average penetration depth of the electrolyte into the bulk. This is evidence for a noticeable degree of short-term protection provided by these coatings, where the increased electrochemical activity and calculated wear-rates are attributed to the sacrificial dissolution of the coating material during initial operation, rather than the consumption of the bulk material.

The Ni–Cr20 coating did not express this behaviour, possessing the highest apparent kinetics of metal and oxide dissolution, the highest wear-rate and the least compact corrosion scale in large part due to its catastrophic enhancement of the NiO → NiF_2 corrosion pathway. This behaviour was avoided by the Ni coated anodes via the rapid interdiffusion of the coating and substrate elements reducing local Ni-enrichment and facilitating Fe-oxidation. In comparison to the base $Ni_{42}Fe_{38}Cu_{20}$ alloy, the coated Cr and Ni variants were seen to reduce corrosion scale blistering and pore formation in the substrate directly beneath the scale, demonstrating positive effects on the resultant structure.

While the Cr and Ni coatings demonstrated signs of superior substrate protection within the first hour of operation, the rapid depletion of the coating suggests that long-term corrosion resistance may eventually revert to that of the base composition. Future studies should focus on extending coating longevity through pre-oxidation treatments — to stabilise the [oxide + coating] interface — or through the investigation of more insoluble coating constituents that can better facilitate the prolonged formation of the protective nickel ferrite ($NiFe_2O_4$) spinel.

CRediT authorship contribution statement

Thomas Jamieson: Writing – review & editing, Writing – original draft, Visualization, Investigation, Formal analysis, Conceptualization. **Ronja Anton:** Writing – review & editing, Writing – original draft, Visualization, Methodology, Investigation, Formal analysis, Conceptualization. **Andrey Yasinskiy:** Writing – original draft, Methodology, Investigation, Formal analysis. **Roman Düssel:** Supervision, Resources. **Ralf Busch:** Writing – review & editing, Supervision, Resources. **Uwe Schulz:** Writing – review & editing, Supervision, Resources. **Bernd Friedrich:** Supervision, Resources. **Isabella Gallino:** Writing – review & editing, Supervision, Resources, Conceptualization.

Declaration of competing interest

The authors declare that they have no known competing financial interests or personal relationships that could have appeared to influence the work reported in this paper.

Acknowledgements

For the technical support at the DLR – German Aerospace Center the authors thank A. Handwerk, R. Nodeh-Farahani and J. Brien as well as E. Wiesner and J. Müller. The authors would also like to thank the Chair of Metallic Materials at Saarland University for long-term collaboration and technical support. This work was carried out within the framework of ongoing research activities at the Technical University of Berlin, the German Aerospace Center (DLR), and TRIMET Aluminium SE. No specific external grant funding was received for this study.

Data availability

The data that support the findings of this study are available from the corresponding author upon reasonable request.

References

[1] International Aluminium Institute, Primary aluminium production, 2024, https://international-aluminium.org/statistics/primary-aluminium-production. (Accessed 23 July 2025).
[2] A.S. Yasinskiy, S.K. Padamata, P.V. Polyakov, A.S. Samoilo, A.V. Suzdaltsev, A.Y. Nikolaev, Electrochemical behaviour of Cu-Al oxygen-evolving anodes in low-temperature fluoride melts and suspensions, in: A. Tomsett (Ed.), Light Metals 2020, 2020, pp. 591–599, http://dx.doi.org/10.1007/978-3-030-36408-3_81.
[3] S. Helle, B. Brodu, B. Davis, D. Guay, L. Roué, Influence of the iron content in Cu–Ni based inert anodes on their corrosion resistance for aluminium electrolysis, Corros. Sci. 53 (2011) 3248–3253, http://dx.doi.org/10.1016/j.corsci.2011.05.069.
[4] T.R. Beck, A non-consumable metal anode for production of aluminum with low-temperature fluoride melts, Light Met. 69 (1995) 355–360.
[5] I. Gallino, Phase Diagram, Thermal Stability, and High Temperature Oxidation of the Ternary Cu-NI-FE System (Ph.D. thesis), Oregon State University, 2004.
[6] I. Gallino, M.E. Kassner, R. Busch, Oxidation and corrosion of highly alloyed Cu–Fe–Ni as inert anode material for aluminum electrowinning in as-cast and homogenized conditions, Corros. Sci. 63 (2012) 293–303, http://dx.doi.org/10.1016/j.corsci.2012.06.013.
[7] K. Singh, G.M. Haarberg, A.R. Mallah, G. Gunnarsson, T. Jamieson, I. Gallino, G. Saevarsdottir, Overpotential on oxygen-evolving platinum and Ni-Fe-Cu anode for low-temperature molten fluoride electrolytes, JOM 76 (2024) 3284–3293, http://dx.doi.org/10.1007/s11837-024-06425-5.
[8] G. Saevarsdottir, G.M. Haarberg, M. Bourmaud, K. Singh, S.K. Padamata, Anodic behaviour of $Ni_{42}Fe_{38}Cu_{20}$ electrode in molten fluoride salts, Electrochem. Soc. 170 (2023) 072508, http://dx.doi.org/10.1149/1945-7111/ace5e3.
[9] X. Zhang, G. Yao, Y. Liu, J. Ma, Z. Zhang, Effects of the additive ZrO_2 on properties of nickel ferrite cermet inert anode, in: S.J. Lindsay (Ed.), Light Metals 2011, 2011, pp. 1129–1134, http://dx.doi.org/10.1007/978-3-319-48160-9_191.
[10] H. He, H. Xiao, K. Zhou, Effect of additive BaO on corrosion resistance of xCu/(10NiO-$NiFe_2O_4$) cermet inert anodes for aluminum electrolysis, Trans. Nonferr. Met. Soc. China 21 (2011) 102–108, http://dx.doi.org/10.1016/S1003-6326(11)60684-5.

[11] Z. Zhigang, X. Jianrong, Sintering kinetics and properties of $NiFe_2O_4$-based ceramics inert anodes doped with TiN nanoparticles, Int. J. Appl. Ceram. Technol. 20 (2023) 329–340, http://dx.doi.org/10.1111/ijac.14231.
[12] L. Cassayre, T.A. Utigard, S. Bouvet, Visualizing gas evolution on graphite and oxygen-evolving anodes, JOM 54 (2002) 41–45, http://dx.doi.org/10.1007/BF02701696.
[13] A.M. Popescu, Current efficiency obtained with SnO_2-based inert anodes in laboratory aluminium cell, Z. Naturforsch. A 56 (2001) 735–738, http://dx.doi.org/10.1515/zna-2001-1106.
[14] R. Galasiu, Inert anodes for aluminium electrolysis: Variation of the properties of nickel ferrite ceramics as a function of the way of preparation, in: Proc. 11th Int. Al. Symp, 2001, pp. 19–22.
[15] T.R. Beck, C.M. Macrae, N.C. Wilson, Metal anode performance in low-temperature electrolytes for aluminum production, Met. Mater. Trans. B 42 (2011) 807–813, http://dx.doi.org/10.1007/s11663-011-9511-8.
[16] I. Galasiu, R. Galasiu, J. Thonstad, Inert Anodes for Aluminium Electrolysis, first ed., Aluminium-Verlag, Düsseldorf, 2007.
[17] A. Yasinskiy, T. Jamieson, K. Singh, G. Gunnarsson, J. Magnusson, D. Feldhaus, R. Düssel, I. Gallino, B. Friedrich, Correlation between corrosion rate and electrochemical parameters of anode process on the metallic electrode in molten oxyfluorides, Light Met. (2024) 596–601.
[18] S.K. Padamata, K. Singh, G.M. Haarberg, G. Saevarsdottir, Anodic behavior of $Ni_{48}Fe_{47}Cu_5$ and $Ni_{42}Fe_{38}Cu_{20}$ in potassium-rich NaF-KF-AlF_3-Al_2O_3 melts, JOM 76 (2024) 3275–3283, http://dx.doi.org/10.1007/s11837-024-06512-7.
[19] E. Gavrilova, G. Goupil, B. Davis, D. Guay, L. Roué, On the key role of Cu on the oxidation behavior of cu–ni–fe based anodes for al electrolysis, Corros. Sci. 101 (2015) 105–113, http://dx.doi.org/10.1016/j.corsci.2015.09.006.
[20] V. Jalilvand, S. Mohammadkhani, F.B. Ettouil, L. Roué, A. Dolatabadi, D. Guay, C. Moreau, The effect of bond coat on the high-temperature behavior of HVOF-sprayed (Co, Ni)O coating on Cu-Ni-Fe anodes, Surf. Coat. Technol. 441 (2022) 128576, http://dx.doi.org/10.1016/j.surfcoat.2022.128576.
[21] V. Jalilvand, Thermal Spray Coating Development of Inert Anode for Aluminum Electrolysis Process (Ph.D. thesis), Concordia University, 2022.
[22] J.A. Thornton, The microstructure of sputter-deposited coatings, J. Vac. Sci. Technol. A 4 (1986) 3059–3065, http://dx.doi.org/10.1116/1.573628.
[23] L. Jordan, W.H. Swanger, The properties of pure nickel, Bureau Stand. J. Res. 5 (1930) 1291–1307.
[24] D.S. Bloom, J. Putman, N. Grant, Melting point and transformation of pure chromium, JOM 4 (1952) 626.
[25] M.M. Hawkeye, M.J. Brett, Glancing angle deposition: Fabrication, properties, and applications of micro- and nanostructured thin films, J. Vac. Sci. Technol. A 25 (2007) 1317–1335, http://dx.doi.org/10.1116/1.2764082.
[26] T. Jamieson, D. Apel, A. Yasinskiy, R. Düssel, P. Decker, et al., On the long-term oxidation behaviour of homogeneous Ni-Fe-Cu alloys for CO_2-free aluminium electrowinning applications at 800°C, J. Mater. Sci. (2025) http://dx.doi.org/10.1007/s10853-025-11313-7.
[27] D. Caplan, G.I. Sproule, Effect of oxide grain structure on the high-temperature oxidation of Cr, Oxid. Met. 9 (1975) 459–472, http://dx.doi.org/10.1007/BF00612672.
[28] E. Epifano, D. Monceau, Ellingham diagram: A new look at an old tool, Corros. Sci. 217 (2023) 111113, http://dx.doi.org/10.1016/j.corsci.2023.111113.
[29] V. Jalilvand, S. Mohammadkhani, F.B. Ettouil, L. Roué, A. Dolatabadi, D. Guay, C. Moreau, The effect of bond coat on the high-temperature behavior of HVOF-sprayed (Co, Ni)O coating on Cu-Ni-Fe anodes, Surf. Coat. Technol. 441 (2022) 128576, http://dx.doi.org/10.1016/j.surfcoat.2022.128576.
[30] A. Ul-Hamid, Diverse scaling behavior of the Ni–20Cr alloy, Mater. Chem. Phys. 80 (2003) 135–142, http://dx.doi.org/10.1016/S0254-0584(02)00472-7.
[31] X. Yaxin, Y. Wang, C. Zeng, Electrochemical studies of the corrosion of pure Fe, Ni and Cr in molten (Li, Na, K)F, High Temp. Mater. Process. 33 (2013) http://dx.doi.org/10.1015/htmp-2013-0071.
[32] P. Asghari-Rad, N. Smith, S. Kim, F. Shi, H. Kim, Electrochemical stability and corrosion behavior of Ni-Cr alloy in molten LiCl-KCl salt, Electrochim. Acta 532 (2025) 146507, http://dx.doi.org/10.1016/j.electacta.2025.146507.
[33] P. Asghari-Rad, N. Smith, S. Kim, F. Shi, H. Kim, Evolution of micro-pores in Ni–Cr alloys via molten salt dealloying, Sci. Rep. 12 (2022) 20785, http://dx.doi.org/10.1038/s41598-022-20286-5.
[34] D. Šuleková, V. Danielik, P. Fellner, J. Thonstad, Solubility of chromium(III) oxide in the molten cryolite system, Metall. Mater. Trans. B 44 (2013) 328–331, http://dx.doi.org/10.1007/s11663-012-9788-2.
[35] K. Singh, T. Jamieson, G. Gunnarsson, G. Haarberg, I. Gallino, R. Busch, J. Magnusson, G. Saevarsdottir, Ni–Fe-based alloy as oxygen evolving anode for sustainable aluminum production, Electrochim. Acta 552 (2026) 148195, http://dx.doi.org/10.1016/j.electacta.2026.148195.
[36] S. Helle, M. Pedron, B. Assouli, B. Davis, D. Guay, L. Roué, Structure and high-temperature oxidation behaviour of Cu–Ni–Fe alloys prepared by high-energy ball milling for application as inert anodes in aluminium electrolysis, Corros. Sci. 52 (10) (2010) 3348–3355, http://dx.doi.org/10.1016/j.corsci.2010.06.011.